1. Experimental and analytical procedure

Starting compositions

We synthesized a series of Fe-rich haplo-basalt (HB) glasses based on the natural Adirondack-class Humphrey basalt from Gusev Crater, Mars (1) as well as a haplo-MORB (B14) and a haplo-andesite (A05) based on the compositions of Armstrong et al. (2) and Zhang et al. (3), respectively. We mixed pre-dried spectroscopically pure SiO_2, Al_2O_3, MgO, $CaCO_3$, Na_2CO_3, and K_2CO_3 reagents. The mixtures were decarbonated by slow heating (3 °C/min), then fused in air for 2 h at 1400 °C in platinum crucibles in a 1 atm furnace. Melts were quenched to glass in water, then crushed and ground in PULVERISETTE agate jars to produce a fine 1–2 μm powder. After decarbonation of the glass powder, Fe was added as Fe_2O_3 powder. The Fe-bearing mixtures were then reduced in a Nabertherm furnace at 900 °C and log $fO_2 = -14$ for 48 h. Finally, nitrogen was introduced as Si_3N_4 powder to yield charges of 0.2 and 0.8 wt% N in the starting material. By varying the amount of Si_3N_4 added to the starting compositions, we were able to change (but not control) the sample fO_2, since Si_3N_4 has a strong reducing effect (1). $Si_3{}^{14}N_4$ was synthetized by Si nitridation using flowing N_2 in a Nabertherm 1 atm furnace. Except for the haplo-MORB sample, starting mixes were spiked in ^{15}N using $Si_3{}^{15}N_4$ synthetized by Leonova et al. (4). The starting materials were loaded into graphite capsules, chosen to ensure reducing conditions and to provide a source of C in the experiments.

Experimental procedure

Experiments were designed to equilibrate graphite-saturated basaltic melts with Fe-C-N alloys over a range of redox conditions (ΔIW −0.5 to ΔIW −3) to determine metal-silicate N fractionation. Experiments were performed in a 3/4-inch piston cylinder at 1 GPa and 1400 °C for 6 h at the Laboratoire Magmas et Volcans (Clermont-Ferrand, France). Run temperature was controlled to within ~1 °C of the set point using W95Re5/W74Re26 thermocouples. Power output was monitored during the runs to ensure no temperature drift. Before decompression, the power to the furnace was cut and the experiment was quenched rapidly (~50 °C/s).

Samples were mounted in epoxy resin and polished individually to limit ^{15}N contamination between samples. They were then removed from the resin and pressed into high-purity indium metal mounts (as recommended for water analysis) and carbon coated for electron microprobe analysis. Raman analyses were performed before carbon coating to avoid interference from carbon vibrational bands.

Electron probe microanalysis (EPMA)

Major element compositions were analyzed with a CAMECA SX5 at CAMPARIS Centre at Sorbonne Université (Paris, France). For silicate glass analyses, we used an accelerating voltage of 10 kV and a 10 nA beam defocused to 10 μm. Diopside glass (Si, Ca, Mg),

43 orthoclase (Al, K), albite (Na), and pure Fe were used as standards. For metal alloys, we used
44 a 10 kV accelerating voltage and a focused 40 nA beam. Pure Fe and Pt were used as metal
45 standards. The major element compositions of silicate glasses are presented in Table S1, and
46 those of metal alloys in Table S2.
47
48 **Table S1.** Major element compositions (wt%) of glasses determined by EPMA.

Sample	n_{EPMA}	SiO_2	Al_2O_3	MgO	CaO	K_2O	FeO	Na_2O	Total
HB01	7	68.7 ± 0.3	8.3 ± 0.4	8.2 ± 0.5	2.4 ± 0.2	0.53 ± 0.06	1.6 ± 0.2	5.3 ± 0.2	95.0 ± 1.2
HB05	4	46.4 ± 0.2	9.1 ± 0.2	10.0 ± 0.3	6.1 ± 0.1	0.74 ± 0.03	22.1 ± 0.6	3.7 ± 0.2	98.2 ± 1.0
HB15	7	61.4 ± 0.4	6.7 ± 0.1	8.0 ± 0.3	3.2 ± 0.1	0.27 ± 0.02	10.5 ± 0.4	5.9 ± 0.3	96.0 ± 1.8
HB3	8	64.8 ± 1.0	3.8 ± 0.2	9.5 ± 0.7	1.84 ± 0.07	0.35 ± 0.08	6.9 ± 0.4	3.9 ± 0.9	91.1 ± 0.9*
HB4	10	60.3 ± 0.9	5.5 ± 0.3	6.9 ± 0.3	3.1 ± 0.1	0.39 ± 0.03	9.2 ± 0.3	4.7 ± 1.0	90.2 ± 0.7*
A05	7	66.7 ± 1.1	13.7 ± 0.7	2.0 ± 0.1	5.9 ± 0.2	1.4 ± 0.1	4.6 ± 0.3	5.4 ± 0.4	99.7 ± 0.6
B14	9	52.4 ± 0.9	15.7 ± 0.2	9.2 ± 0.3	11.5 ± 0.1	0.06 ± 0.03	7.5 ± 0.6	2.2 ± 0.2	98.5 ± 1.0

49 *Low totals may be due to graphite microinclusions in the samples.
50 n_{EPMA} indicates the number of EPMA analyses on each sample.
51 Reported uncertainties are 1σ standard deviations.
52
53 **Table S2.** Fe and Pt contents of metal alloys determined by EPMA, and their N and C contents
54 determined by SIMS.

Sample	n_{EPMA}	Fe [wt%]	Pt [wt%]	n_{SIMS}	C [wt%]	N [ppm]
HB01	5	93.7 ± 0.7	0.07 ± 0.08	2	0.110 ± 0.001	28 ± 3
HB05	5	93.6 ± 1.2	0.7 ± 0.4	4	6.06 ± 0.01	1571 ± 1287
HB15	2	89.6 ± 0.1	bdl	3	2.66 ± 0.06	682 ± 267
HB3	5	92.2 ± 3.2	0.2 ± 0.4	4	5.74 ± 0.01	1493 ± 149
HB4	11	97.1 ± 1.5	0.1 ± 0.6	6	5.73 ± 0.02	1488 ± 14
A05	6	93.4 ± 0.2	0.6 ± 0.8	3	2.552 ± 0.001	669 ± 125
B14	7	94.6 ± 1.2	bdl	3	7.42 ± 0.01	1012 ± 20

55 bdl: below detection limit.
56 n_{EPMA} and n_{SIMS} indicate the number of EPMA and SIMS analyses, respectively.
57 Reported uncertainties are 1σ standard deviations for Fe and Pt contents and 2σ standard deviations
58 for C and N contents.
59

Raman spectroscopy

61 For silicate glasses, Raman spectrosocopy measurements were carried out using a LabRAM
62 HR microspectrometer (Horiba Jobin Yvon) at GeoRessources (Nancy, France) using the
63 457.9 nm radiations of an Ar+ laser (Stabilite 2017, Spectra-Physics) with 100–155 mW
64 output. The laser intensity was reduced with neutral density filters to avoid thermal
65 degradation of the samples and focused to a ~2 μm spot size with 8–23 mW on sample
66 through a 50× long-working-distance Olympus objective with a 0.5 numerical aperture.
67 Scattered light was collected through a confocal aperture into a focal length of 800 mm. The
68 spectrometer was equipped with an 1800 grooves·mm^{-1} grating. Acquisition time was 10 s,
69 with 60 acquisitions collected per spectrum. Raman intensities were corrected from the
70 instrument response curve by calibration of the spectrometer toward a white lamp (5). To
71 observe molecular N_2 vibrations, spectra were acquired in the 2200–2400 cm^{-1} spectral

72 window. C-H, N-H, and O-H vibrations were observed in the 2800–3700 cm^{-1} spectral
73 window.
74   For metal alloys, we used a LabRAM microspectrometer (Horiba Jobin Yvon) at
75 GeoRessources. Sample excitation was accomplished using the 514.5 nm line of an Ar+ laser
76 with 100–155 mW output. To avoid melting the metal, the laser intensity was reduced with
77 neutral density filters to between 9 and 15 mW. Measurements were performed using an 1800
78 grooves·mm^{-1} grating centered at 950 cm^{-1}. Ten acquisitions of 10 s were collected.
79   Baseline corrections were performed using the IGOR software package (Wavemetrics
80 Inc.). A linear baseline was used for the 2200–2400 cm^{-1} part of the Raman signal of silicate
81 glasses, whereas a spline correction was fitted for the 2800–3700 cm^{-1} baseline of silicate
82 glasses and the 200–900 cm^{-1} part of the Raman signal in metal alloys.
83
84 **Secondary ion mass spectrometry (SIMS)**
85 *In-situ* measurements of N concentrations and isotopic ratios were performed at the Centre de
86 Recherches Pétrographiques et Géochimiques (CRPG, Nancy, France) using the CAMECA
87 1280 HR2 and 1270 ion microprobes for silicate glasses and metal blobs, respectively.
88 Sample mounts were coated with gold and left in the instrument airlock for at least 24 h to
89 ensure thorough removal of any adsorbed water before introduction into the sample chamber,
90 although any hydride species are well-resolved from the peaks of interest (6). Furthermore, to
91 minimize any surface contamination, the surface of the glasses and metals were pre-sputtered
92 for 180 s over an area of 10 μm × 10 μm prior to signal acquisition. For all abundance and
93 isotopic analyses, the beam was rastered over an area of 5 μm × 5 μm (**Fig. S1**), and a
94 dynamical transfer operating system was used to compensate the primary rastering by
95 recentering the beam in the secondary optic of the ion probe. Prior to data acquisition, the
96 secondary ion beam was automatically centered in *x* and *y* on the field aperture and the
97 contrast aperture, followed by a mass-centering routine in order to compensate for any
98 magnetic field drift.
99   Nitrogen isotopes in silicate glasses (Table S3) were measured on the CAMECA 1280
100 HR2 ion microprobe by spot analyses of $^{14}N^{16}O^-$ and $^{15}N^{16}O^-$ molecular ions at masses 30 and
101 31, respectively, at a nominal mass resolution $m/\Delta m = 14,000$ using a 10 kV Cs$^+$ primary ion
102 beam, a ~10 nA current, and a normal-incidence electron gun for charge compensation (6).
103 The $^{14}N^{16}O^-$ and $^{15}N^{16}O^-$ ions were measured for 25 cycles in peak-jumping mode on an
104 electron multiplier for 4 and 20 s, respectively, together with $^{27}Al^-$ (4 s), $^{30}Si^-$ (4 s), and $^{16}O_2^-$
105 (4 s) on a faraday cup. A suite of 12 reference glasses with known ^{14}N contents (6) was used
106 to determine the nitrogen concentration of the samples based on the $^{14}N^{16}O^-$ count rate
107 normalized by the $^{16}O_2^-$ signal (**Fig. S2a**). Based on repeated isotope ratio measurements in 5
108 out of the 12 reference glasses (with N content ≥ 136 ppm) with $\delta^{15}N = -4 \pm 1‰$ (6), the
109 instrumental mass fractionation (IMF) for glass analyses was determined to be $\alpha_{inst} = 1.0259$
110 ± 0.0074 (2σ). Thus, the measured $^{15}N/^{14}N$ ratios of the experimental glasses were
111 subsequently corrected for IMF according to $(^{15}N/^{14}N)_{corr} = (^{15}N/^{14}N)_{measured} / \alpha_{inst}$.
112
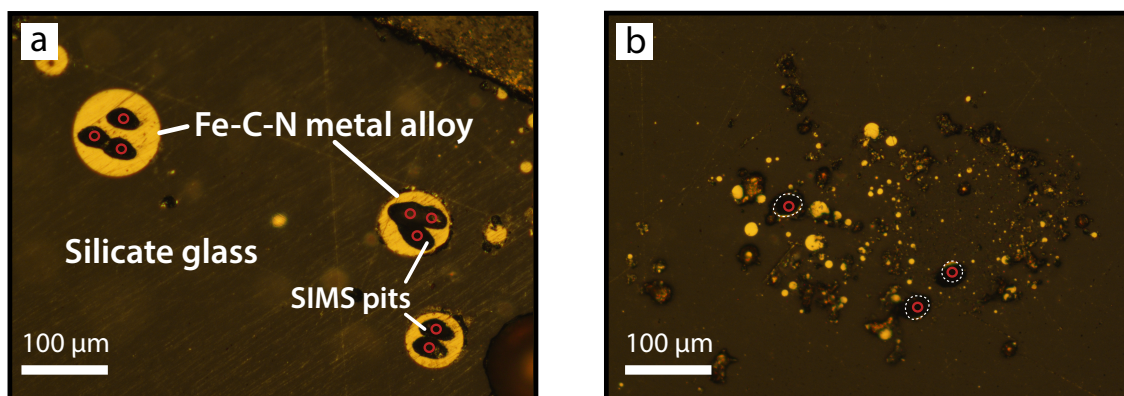
113
114 **Fig. S1.** Reflected-light microscope images of (a) sample HB3 and (b) sample A05 showing the
115 variable sizes of metal alloy blobs among different samples. Red circles (~5 µm) indicate the location
116 of ion probe spots for metal C-N measurements. The surrounding black spots are the area where the
117 gold coating was removed due to primary ion beam sputtering. The white dotted circles in (b)
118 represent the initial shapes of the metal blobs.

119
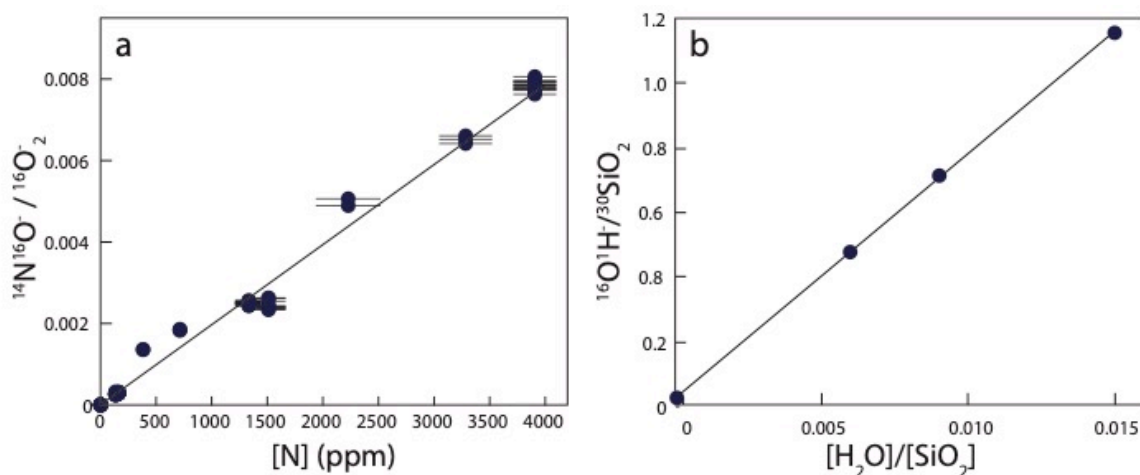
120
121 **Fig. S2.** Calibration lines for N and OH abundance analyses in silicate glasses. (a) The relationship
122 between the secondary ion intensity ratio $^{14}N^{16}O^-/^{16}O_2^-$ and the known ^{14}N content of the reference
123 glasses ($r^2 = 0.95$). (b) The measured and reference values of H_2O and SiO_2 concentrations in the four
124 glass reference materials provide excellent consistency ($r^2 = 0.99$).

125

126   Nitrogen and carbon concentrations, as well as $^{15}N/^{14}N$ and $^{13}C/^{12}C$, in the metal blobs
127 were measured with the CAMECA 1270 ion microprobe using a 10 kV Cs$^+$ primary ion
128 beam, a ~2.4 nA current, and a normal-incidence electron gun for charge compensation. The
129 size of the primary beam was set to ~5 µm to analyze metal blobs 10–65 µm in diameter (Fig.
130 S1). Nitrogen isotopes (Table S3) were measured as $^{12}C^{14}N^-$ and $^{12}C^{15}N^-$ at masses 26 and 27,
131 respectively, with a mass resolution of 8,000. Twelve cycles were collected for each analysis,
132 following the mass sequence $^{12}C_2^-$ (8 s), $^{12}C^{13}C^-$ (16 s), $^{12}C^{14}N^-$ (8 s), $^{13}C^{14}N^-$ (8 s), $^{12}C^{15}N^-$ (8
133 s), $^{28}Si^-$ (8 s), and $^{56}Fe^-$ (8 s). With the exception of $^{12}C^{13}C$, signals were measured on a
134 faraday cup in most cases. For samples HB3 and HB4, $^{13}C^{14}N$ was measured on the electron
135 multiplier. Because the metal blobs of sample HB01 contained only 28 ppm N, $^{12}C^{14}N$,
136 $^{12}C^{15}N$, and $^{13}C^{14}N$ were measured on the electron multiplier. Carbon and nitrogen elemental
137 abundances were determined using the ^{12}C signal and the $^{12}C^{14}N/^{12}C$ ratio, respectively.

138　Carbon concentrations were calibrated using a set of four certified NBS stainless steel
139　reference materials (NBS661, NBS662, NBS663, and NBS664), containing between 0.16 and
140　0.87 wt% C (**Fig. S3a**). Nitrogen concentrations were determined using the certified standard
141　NBS662 ($^{12}C^{14}N/^{12}C \geq 0.03$) and sample B14 (**Fig. S3b**), for which the N content and $\delta^{15}N$
142　value were independently measured by noble gas static mass spectrometry (see below).
143　NBS661, NBS663, and NBS664 were not used for N analyses because the uncertainties on
144　their $^{12}C^{14}N/^{12}C$ ratios were greater than or equal to the measured values, likely due to a
145　highly heterogeneous nitrogen distribution in these stainless steel samples. Although only two
146　metallic calibrants were used to derive the N content in metals, the calibration is reliable since
147　partition coefficients calculated from these values are consistent with literature data (~150
148　data points, Fig. 1 in the main text).
149
150　**Table S3.** $^{15}N/^{14}N$ ratios (corrected for IMF) determined by SIMS in silicate glasses and metal blobs.

Sample	n_{SIMS} silicate	$^{15}N/^{14}N^{silicate}$	n_{SIMS} metal	$^{15}N/^{14}N^{metal}$
HB01	3	0.091 ± 0.001	2	0.070 ± 0.006
HB05	3	0.685 ± 0.011	4	0.652 ± 0.007
HB15	3	8.197 ± 0.140	3	7.298 ± 0.364
HB3	3	0.828 ± 0.001	4	0.724 ± 0.004
HB4	3	0.864 ± 0.002	6	0.790 ± 0.005
A05	3	0.672 ± 0.001	3	0.656 ± 0.001
Reference material				
B14[*]	–	nd	3	0.003725 ± 0.000049

151　[*]B14 served as a calibrant for N analyses in metal; its $^{15}N/^{14}N^{silicate}$ was not determined (nd).
152　The reproducibility on B14 SIMS measurements is 1.3%.
153　n_{SIMS} indicates the number of SIMS analyses.
154　Reported uncertainties are 2σ standard deviations.
155
156　　　　Sample B14 was also analyzed by noble gas mass spectrometry. Thus, we were able to
157　directly measure the N isotopic compositions (relative to the atmosphere) of its metal blobs
158　($\delta^{15}N^{metal} = -12 \pm 1$‰). Based on these independent isotope ratio measurements of B14, the
159　IMF of the ion probe during metal analysis was determined to be $\alpha_{inst} = 1.0251 \pm 0.0859$ (2σ).
160　Thus, the measured $^{15}N/^{14}N$ ratios of all the metal phases in the Fe-rich basalt and andesite
161　samples were subsequently corrected for IMF according to $(^{15}N/^{14}N)_{corr} = (^{15}N/^{14}N)_{measured} /$
162　α_{inst}.
163
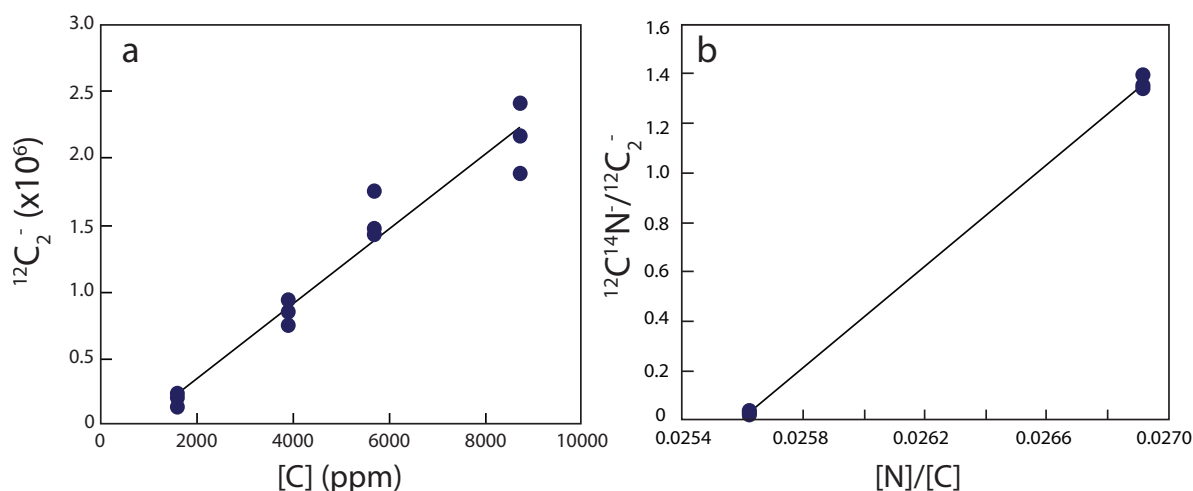
Fig. S3. Calibration lines for C and N abundance analyses in metal alloys. (a) The relationship between the secondary ion intensity ratio $^{12}C_2^-$ and the known C content of the NBS stainless steel reference materials ($r^2 = 0.95$). (b) The relationship between the secondary ion intensity ratio $^{12}C^{14}N^-/^{12}C^-$ and the known N/C ratio of NBS662 and sample B14 ($r^2 = 0.99$).

Hydrogen abundances in silicate glasses were measured with the CAMECA 1280 HR2 ion microprobe. A liquid-nitrogen cold trap was used to reduce the H_2O background and maintain a pressure below 2×10^{-9} Torr in the analytical chamber. A 10 kV Cs^+ primary ion beam was used for the analyses. Prior to analysis, a 180-s high-current (1 nA) presputtering was rastered over an area of 20 μm × 20 μm to remove the gold coating and reach the sputtering steady state. The samples were then sputtered with a current of 350 pA rastered over an area of 10 μm × 10 μm and a normal-incidence electron gun was used for charge compensation. A small field aperture (1000 μm) and a high magnification (40 μm maximum area) were used to restrict the analytical areas to 5 μm × 5 μm and eliminate hydrogen contamination from the crater edges. The $^{12}C^-$, $^{16}OH^-$, and $^{29}Si^-$ ions were collected sequentially by changing the magnetic field and counted with a monocollection electron multiplier. The mass resolution was set to 7,000 to avoid interferences of $^{17}O^-$ on $^{16}OH^-$ and $^{28}SiH^-$ on $^{29}Si^-$. The H_2O concentrations of the experimental glasses were determined using the calibrated relationship between the secondary ion intensity ratios $^{16}OH^-/^{29}Si^-$ and the known H_2O abundances of four glass standards (**Fig. S2b**): KL2-G [0.015 wt% H_2O (7)], VG-2 [0.28 wt% H_2O (8)], M48 [0.77 wt% H_2O (9)], and MC84-df [0.707 wt% H_2O (10)].

Noble gas mass spectrometry

Nitrogen abundances and isotopic ratios in sample B14 were determined by CO_2 laser extraction static mass spectrometry at the CRPG noble gas analytical facility (11). Samples were cleaned in an ultrasonic bath filled with acetone, then weighed and loaded into different pits of the laser chamber. Analyses were carried out on a 36-μg metal alloy blob and on a 21-μg fragment of silicate glass (free of visible graphite from the capsule or graphite inclusions, as observed under the microscope). The samples were heated individually with a continuous-mode infrared CO_2 laser mounted on an *x-y* stage. Samples were reheated after melting to verify that their N was completely extracted during the first heating step. After gas

196 purification (11), nitrogen isotopic data were collected on a Noblesse HR noble gas mass
197 spectrometer. The Noblesse HR at CRPG is equipped with three Faraday cups and four ion
198 counter collectors, thus allowing nitrogen isotopes to be measured in multi-collection mode;
199 this method provides more precise and reproducible data than those obtained previously in
200 mono-collection mode on the VG5400 noble gas mass spectrometer by Li et al. (12). The
201 analytical procedure consisted of first measuring the $^{12}C^{16}O$ signal, followed by the $^{12}C^{16}O$ +
202 $^{14}N^{14}N$ and $^{13}C^{16}O$ + $^{14}N^{15}N$ signals using two Faraday cups ($R = 10^{11}$ Ω). After data
203 acquisition, which consisted of 25 cycles, the $^{14}N^{14}N$ and $^{15}N^{14}N$ intensities were corrected for
204 the CO contribution. Calibrated air aliquots were used to determine the analytical sensitivity
205 (1.7×10^{-4} A/Torr) and the reproducibility of abundance (±1.9%, 1σ) and isotope ratio
206 measurements (±0.06%, 1σ).
207
208   **2. Relationship between fO$_2$, melt structure, and N isotopic fractionation**
209
210 The precipitation of Fe metal in various proportions, depending on fO$_2$, causes a change in
211 melt structure (Figs. S4a and S5). As previously noted by Dalou et al. (1) and Armstrong et al.
212 (2), silicate glasses, for example, become more Si-rich and Fe-poor relative to the starting
213 compositions owing to oxidation of added Si$_3$N$_4$ and reduction of FeO in the melt with
214 decreasing fO$_2$. These changes in the mole fractions of Si and Fe with decreasing fO$_2$ result in
215 an increase in melt polymerization (i.e., a decrease of NBO/T, the ratio of non-bridging
216 oxygens to tetrahedrally coordinated cations).
217   Melt polymerization does not directly affect N isotopic fractionation. If the increase
218 in melt polymerization was the dominant control, the N isotopic fractionations in samples
219 HB3 and A05, which had a similar Fe fraction and NBO/T after the experiment, should have
220 had similar Δ^{15}N or Δ^{15}N* values. However, they show distinct Δ^{15}N values of −135 ± 1‰
221 and −25 ± 1‰, respectively. Similarly, as the melts become more polymerized, their Δ^{15}N or
222 Δ^{15}N* values should decrease. In both cases, this is not what we observe (Fig. S4b).
223   In the main text, we argue that the dependence of N isotopic fractionation on fO$_2$ can
224 be related to variable NH/N$_2$ ratios in the glasses. The NH/N$_2$ ratios in the glasses seem to
225 depend on the initial degree of melt polymerization (for reasons that remain to be explored)
226 and on the fO$_2$ conditions (Fig. S5).
227

228
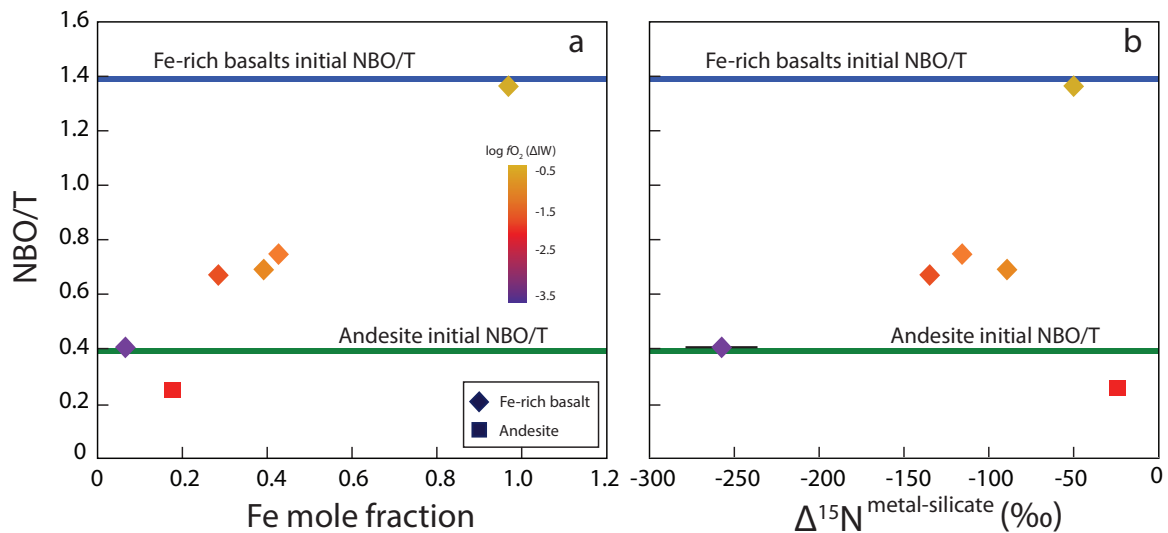
229 **Fig. S4.** NBO/T ratios (lower values being more polymerized) of the glasses as a function of fO_2 (color
230 scale) and (a) Fe mole fraction and (b) $\Delta^{15}N^{metal-silicate}$.

231

232
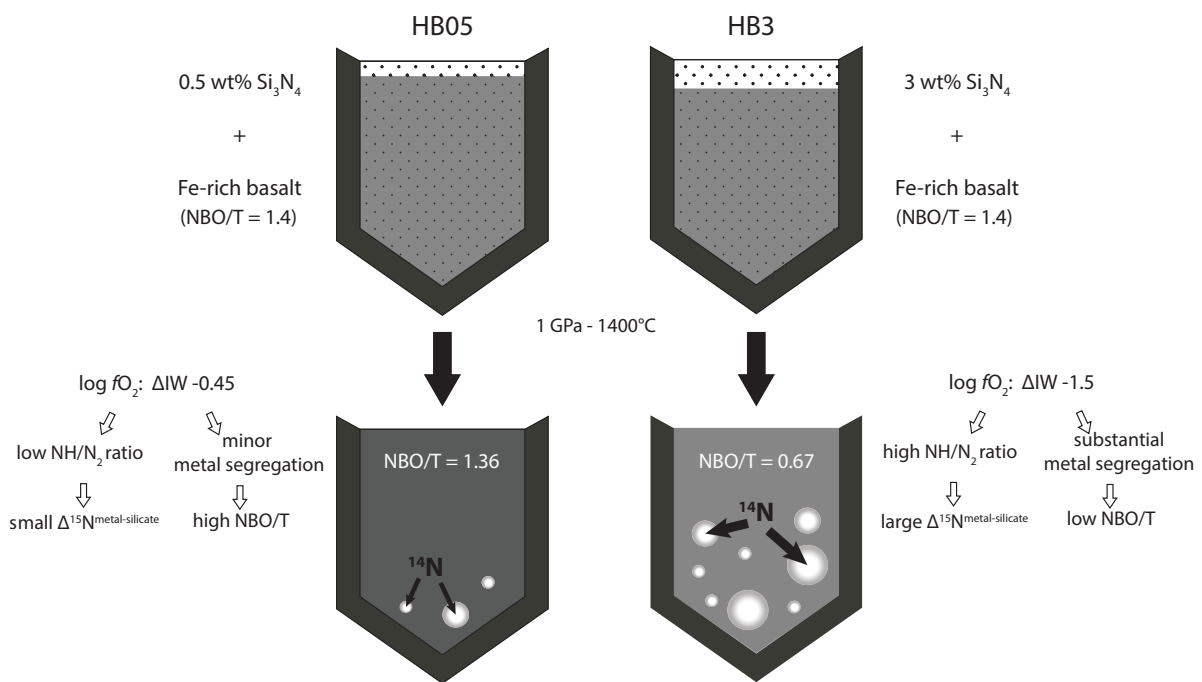
233
234 **Fig. S5.** Schematic representation of the experimental procedure and the direct and indirect effects
235 of fO_2 on metal segregation , the NBO/T and NH/N_2 ratios of the silicate glasses, as well as on the N
236 isotope fractionation between the metal and silicate phases.

237

238

239 **References**

240   1. Dalou C, Hirschmann MM, von der Handt A, Mosenfelder J, Armstrong LS (2017) Nitrogen and carbon
241   fractionation during core–mantle differentiation at shallow depth. *Earth and Planetary Science*
242   *Letters* 458:141-151.

243 2. Armstrong LS, Hirschmann MM, Stanley BD, Falksen EG, Jacobsen SD (2015) Speciation and solubility
244   of reduced C–O–H–N volatiles in mafic melt: implications for volcanism, atmospheric evolution, and
245   deep volatile cycles in the terrestrial planets. *Geochimica et Cosmochimica Acta* 171:283-302.
246 3. Zhang HL, Hirschmann MM, Cottrell E, Newville M, Lanzirotti A (2016) Structural environment of iron
247   and accurate determination of Fe3+/ΣFe ratios in andesitic glasses by XANES and Mössbauer
248   spectroscopy. *Chemical Geology* 428:48-58.
249 4. Leonova E, Grins J, Shariatgorji M, Ilag LL, Edén M (2009) Solid-state NMR investigations of Si-29 and
250   N-15 enriched silicon nitride. Solid state nuclear magnetic resonance, 36(1), 11-18.
251 5. Dubessy J, Caumon M-C, Rull F, Sharma S (2012) Instrumentation in Raman spectroscopy: elementary
252   theory and practice, in: Dubessy, J., Caumon, M.-C., Rull, F. (Eds.), Raman Spectroscopy Applied to
253   Earth Sciences and Cultural Heritage, EMU Notes in Mineralogy. The European Mineralogical Union
254   and the Mineralogical Society of Great Britain & Ireland, London, pp. 83–165.
255 6. Füri E, Deloule E, Dalou C (2018) Nitrogen abundance and isotope analysis of silicate glasses by
256   secondary ionization mass spectrometry. *Chemical Geology* 493:327–337.
257 7. Jochum, K.P. et al. (2006) MPI-DING reference glasses for in situ microanalysis: New reference values
258   for element concentrations and isotope ratios. *Geochemistry, Geophys. Geosystems* 7.
259 8. Sobolev AV, Asafov EV, Gurenko AA, Arndt NT, Batanova VG, Portnyagin MV, Garbe-Schönberg D,
260   Krasheninnikov SP (2016) Komatiites reveal a hydrous Archaean deep-mantle reservoir. *Nature* 531-
261   628–632.
262 9. Shishkina TA, Botcharnikov RE, Holtz F, Almeev RR, Portnyagin MV (2010) Solubility of H_2O- and CO_2-
263   bearing fluids in tholeiitic basalts at pressures up to 500MPa. *Chemical Geology* 277:115–125.
264 10. Hauri E (2002) SIMS analysis of volatiles in silicate glasses, 2: Isotopes and abundances in Hawaiian
265   melt inclusions. *Chemical Geology* 183:115–141.
266 11. Humbert F, Libourel G, France-Lanord C, Zimmermann L, Marty B (2000) CO_2-laser extraction-static
267   mass spectrometry analysis of ultra-low concentrations of nitrogen in silicates. *Geostandards*
268   *Newsletter* 24(2):255-260.
269 12. Li YF, Marty B, Shcheka S, Zimmermann L, Keppler H (2016) Nitrogen isotope fractionation during
270   terrestrial core-mantle separation. Geochemical Perspectives 2
271
272